A Novel Approach for Restoring Lost Details in Pore Network Images based on Pattern Recognition using Generative Adversarial Networks

A. ElahiKhaledi[a], S. Jamshidi[a,*], M. Masihi[a]

a. Department of Chemical and Petroleum Engineering, Sharif University of Technology, Tehran, Iran.

E-mail addresses: alireza.elahi73@sharif.edu (A. ElahiKhaledi); jamshidi@sharif.edu (S. Jamshidi); masihi@sharif.edu (M. Masihi)

Abstract The growing application of unconventional resources and reservoir heterogeneity has highlighted the importance of multi-scale modeling. Recent studies indicate that sub-resolution porosity (SRP) significantly impacts on the flow characteristics of porous media. However, SRP details are often absent in low-quality images, leading to discrepancies between pore network model predictions and experimental results. This study presents a novel approach for restoring lost details in pore network images using RealESRGAN, an advanced generative adversarial network (GAN) model. Traditional techniques like interpolation and filtering have long been used to enhance image resolution, but recent advancements in artificial intelligence, particularly GANs, have revolutionized this field. In petroleum engineering, GANs are utilized in super-resolution tasks, in which they learn to reconstruct high-resolution images from low-resolution inputs. This research employs various sandstone and carbonate rock samples to train the RealESRGAN model and generates synthetic low-resolution datasets from high-resolution images. Compared to earlier models like SRGAN, RealESRGAN demonstrates superior performance. Evaluation metrics, including LPIPS, are used to investigate the quality of the generated images. Finally, pore network model constructed from the generated images closely align with actual models.

Keywords: Pore Network Modeling, Image Resolution, Image Recovery, Pattern Recognition, Generative Adversarial Network, RealESRGAN.

1. Introduction

There is a growing interest in the development of unconventional oil and gas resources because of the depletion of conventional oil and gas resources. These resources are a significant part of the total hydrocarbon resources [1,2]. However, the presence of heterogeneity poses some challenges in the development of such types of reservoirs. This heterogeneity could be at the reservoir scale and the pore scale [3-5]. These are referred to as sub-resolution porosity (SRP) [6]. The larger pores typically control the main flow, however, the SRP also influences the flow characteristics of the porous media even though it has minimal impact on the porosity [6-9].

1.1. Pore Network Modeling

The flow properties of the porous media can be obtained in three ways: using experiments, and employing analytical or numerical models at the pore scale. The experimental method is

relatively simple, but it has its drawbacks, such as measurement errors [10,11], smaller core sizes than the representative element volume (REV) [12], boundary effects [6, 13], damages in samples due to flow measurements [14,15], and the mismatch of the flow regime with the reality of the porous medium [16,17]. Analytical models calculate the flow properties based on the physical parameters of the porous media. Kozeny-Carman (K-C) equation is the most popular analytical model for permeability determination [18]. This model is obtained by approximating the porous media by a bounded capillary model. But this model has many drawbacks, for instance, it takes into account only porosity and specific surface area. This model has been recently updated and contains more details of the geometry of the porous media [19,20]. Even though topology and heterogeneity have a significant impact on the flow properties of porous media, these parameters cannot be taken into account in analytical models. The analytical method has some limitations such as the high computational complexity, the requirement of high-resolution images, the low extensibility, and the difficulty of adjusting the parameters. On the other hand, the pore network models (Simplifying porous media to pores and throats) are relatively faster, more scalable, and flexible in their applicability [17].

With the help of X-ray computer tomography (X-CT) the possibility of numerical modeling of the porous media has been offered in the last few years [21,22]. In this method, hundreds or thousands of two-dimensional images of the rock sample taken at different distances are used to reconstruct the porous media in three dimensions. Usually, the microstructures of porous media reconstructed in such a manner have dimensions of about 1 to several mm^3 and the resolution of the images is up to $1\mu m^3$. Other imaging techniques can also be used including magnetic resonance imaging (MRI), confocal microscopy, optical serial sectioning microscopy (OSSM), focused ion beam-scanning electron microscopy (FIB-SEM), serial block-face scanning electron microscopy (SBF-SEM), and transmission electron microscopy (TEM) [23]. Every one of them has its advantages and disadvantages. The only key differences between these methods are the image resolution and the field-of-view (size of the final model). In general, by increasing the resolution of the images, the dimensions of the final model are reduced and this model may no longer work as a REV. There are some problems in applying imaging techniques in natural rocks. The major challenge is the fact that the pore structure is often heterogeneous and contains different pore sizes. Until recently, it was thought that the flow in SRP is dominated by diffusion and is zero, and hence these pores were omitted in the construction of the model [24-28]. Some of the current research has established that the SRP contributes to enhancing the conductivity of the network through the establishment of links between the bigger pores [8].

The interaction between the total dimension of the network and resolution, combined with the cost of high-resolution imaging, significantly limits the availability of high-resolution images. Thus, it is essential to employ techniques that can improve the quality of existing images to restore the missing details.

Modeling of porous media using images can be performed through different approaches: direct modeling which uses micro-CT or SEM images of the porous medium to reconstruct its structure. In this approach, the porous media is discretized into a network of voxels representing pores and throats within the porous structure [29]. The second method is the pore network model where the porous medium is modeled as a network of pores and throats. This model is used extensively to model the fluid flow through the pore network [17].

The pore network models are computationally effective and can be used for quick simulations and sensitivity analyses. It also needs fewer input data and is applicable for multiphase flow and other processes such as wetting and capillary pressure [17]. However, it loses accuracy when trying to model complex or irregular porous structures. In addition, it fails to describe the nonelementary transport characteristics and can inadequately describe the fine-scale structural heterogeneities in the medium [30]. Based on these assumptions, we employ the pore network modeling approach due to the simplicity of the model and the speed of calculations.

1.2. Increasing Image Quality

Images are important in petroleum engineering for characterization, monitoring, and decision-making, and high-quality images are essential. As mentioned, due to limitations and the lack of high-quality images in porous media, we need to enhance image quality. Enhancing image quality is usually associated with operations like noise reduction, increasing resolution, contrast enhancement, and edge and feature detection [31]. Since image quality enhancement is a rather broad concept, many techniques have been developed over time, from traditional methods to cutting-edge deep learning approaches.

Earlier methods relied on statistical techniques and filtering, which focused on basic improvements, often at the expense of detail preservation. Some of the well-known techniques in this category are Filtering [32], histogram equalization [33], and edge detection [34]. These approaches are not efficient when dealing with complex features and they lead to image quality degradation.

With advances in image processing, there were new methods developed such as single-image super resolution (SISR) and multi-image super resolution (MISR). These methods enhance the level of detail and clarity collectively [35,36]. Such methods as image fusion [37] and deconvolution [38] provide better and more accurate visualization of the original scene and are especially useful in situations where high detail is required. Different techniques are often applied in conjunction, such as combining super-resolution and noise reduction for a clearer final image. These advancements have increased improved image quality by enabling adaptive and fine-tuned adjustments, resulting in clearer, more informative images [39].

Deep learning has introduced a new way of improving image quality. Methods like SRCNN [40], WDSR [41], and EDSR [42] pioneered using deeper CNN architectures to increase upscaling accuracy and detail preservation. SRCNN leverages a convolutional neural network to establish relational mappings between low and high-resolution images. However, a major drawback of conventional CNNs is in the ability to reconstruct complex image textures especially when working at large scale factors [43]. In order to solve this problem, GANs were proposed to be used for image super resolution. A GAN is a modern deep learning algorithm that enables two neural networks to compete with each other in the form of a game with zero sum. This framework can generate artificial graphical samples that are similar and nearly indistinguishable from images in a training set [44]. The super-resolution problem was one of the first to be tackled by the use of Generative Adversarial Networks (GANs) with the development of SRGAN [45]. Recent advancements in super-resolution (SR) techniques include transformer-based methods, diffusion models, and GANs, each tailored to enhance image quality with minimal computational resources [46]. Transformer-based SR models, such as detail-preserving transformers and EPIT, capture intricate spatial and angular details,

especially beneficial in light-field imaging tasks [46]. Diffusion models, like SinSR, streamline the typically lengthy diffusion process by using a one-step distillation method, allowing for faster and more efficient SR without compromising detail (Lei et al., 2024). Meanwhile, GANs continue to evolve, often incorporating perceptual loss functions that improve image realism and fidelity, which are especially useful for 4K video and compressed image upscaling [47]. These innovative approaches offer versatile solutions for high-resolution imaging across various applications. However, GANs are often regarded as the best method due to their superior ability to produce finer details and more realistic images [47].

SRGANs as one of the first GAN-based models use a generative adversarial network to enhance low-resolution images to a higher quality [43]. The SRGAN's architecture consists of a deep convolutional network with a residual block that uses a perceptual loss as its objective function. This objective function contains both adversarial and content loss [48]. The feature loss in this model is determined by measuring the difference between the feature map of the generated image (derived from the pre-trained VGG19 network) and that of the real image. GANs incorporate skip connections within deep residual networks (ResNet) [49]. In SRGAN, similarity between feature maps is assessed using Mean Squared Error (MSE). Additionally, the model leverages the high-level feature map from the VGG network to establish a perceptual loss, combined with a discriminator to produce a result perceptually matching the high-resolution (HR) reference image. Wang et al. [50] proposed ESRGAN as an enhancement to SRGAN, aiming to improve visual output quality. They achieved this by modifying SRGAN's architecture, including the removal of the BN layer and the addition of RDDB blocks to optimize training. The discriminator was further refined by introducing Relativistic GAN (RGAN) for enhanced classification.

Jiang et al. [51] proposed EEGAN, a GAN-based edge-enhancement network, to promote high-frequency edge details in noisy satellite images as well as super-resolution reconstruction enhancement. It employs an Ultra-Dense Subnetwork (UDSN) and Edge-Enhancement Subnetwork (EESN) to enhance contours and suppress noise. Gan et al. [52] proposed udGAN which incorporates Ultra-Dense Residual Blocks and adversarial learning for photorealistic SR even when the degradation is unknown. Tu et al. [53] proposed SWCGAN combines convolution and Swin Transformer layers to achieve better performance than other approaches on the LPIPS measure. Jia et al. [54] introduced MA-GAN with Attention-based Up Sampling (AUP) for high-quality output in the remote sensing application. Finally, Real-ESRGAN proposed a high-order degradation model for realistic image super-resolution without generating over-smoothed images [55].

One of the main disadvantages of the older methods of image enhancement compared with the AI-based methods is the problem of detail loss. Traditional approaches, often struggle with detail preservation and contrast adjustment, especially in high-complexity images. AI-based methods especially deep learning models, have the advantage of being able to automatically adjust the parameters of the algorithm based on the characteristics of the images. Also, these methods are able to learn patterns and adjust to them, which, in general, cannot be said about traditional methods [56].

1.3. Objective of This Paper

In this work, we employed the RealESRGAN as our model for super-resolution tasks. With the help of the developments made in RealESRGAN, we plan to improve the quality of synthetic images and restore the lost details. We use images of a multi-scale microstructure,

including inter and intragrain pores. Using an innovative method, the resolution of the primary images is reduced to investigate the effect of reducing the resolution on the constructed pore network. Pore network model properties, such as the size of pores and throats are extracted using the Snow algorithm. Finally, the RealESRGAN method is used to recover the lost details in the synthetic images.

2. Methodology

2.1. Image Recovery

As stated above, GAN-based methods are employed in the improvement of image quality and in the creation of fake images that are as good as the original images. These networks consist of two main components: The Generator (G) and the discriminator (D). The generator draws a random number from a distribution that is known and preferably easy to model, for example, the Gaussian distribution $p_z(z)$, and tries to generate images that are similar to real ones. This noise is then mapped to the image data space through a differentiable function $G(z;\theta_g)$, where θ_g represents the generator's parameters. The generator tries to produce images $G(z)$ that are like to real images [57].

To overcome the problem of lack of real image pair for each generator output, a discriminator network is used. The discriminator $D(x;\theta_d)$, takes the generated image and tries to differentiate it from the real image extracted from the dataset (θ_d represents the discriminator's parameters). The discriminator returns a scaler value $D(x)$ that shows the probability of x being real. This process assists the generator in enhancing its performance over time. Using the loss function as defined in Eq. (1), the parameters of both generator and discriminator networks (θ_g and θ_d) can be adjusted iteratively through the use of gradient-based optimization techniques like stochastic gradient descent (SGD) until the model converges [57].

$$\min_G \max_D V(G,D) = \mathrm{E}_{x\sim p_{data}(x)}\left[\log D(x)\right] + \mathrm{E}_{z\sim p_z(z)}\left[\log(1-D\left(G\left(z\right)\right)\right] \quad \textbf{(1)}$$

The generator tries to minimize $\log\left(1-D\left(G(z)\right)\right)$ and make the generated images close to real, while the discriminator maximizes $\log\left(D\left(x\right)\right)$ for real images. In the training process, the generator is trained to generate images that are more difficult for the discriminator to say that they are fake. The discriminator is trained to become more effective in the classification of images as being real or fake. This is done in a manner where the two are pitted against each other until the generator is able to produce images that are almost real. Thanks to the generator and discriminator in GAN, it is possible to carry out very powerful image generation and image enhancement that cannot be done with other image processing methods [57].

SRGAN [45] contains a residual block in both the generator and the discriminator, and the generator has skip connections. This architecture is designed to enhance the quality of the generated images by capturing and utilizing the fine details. The primary novelty of SRGAN

is the method of generator initialization: unlike GANs that are initialized with noise, the generator of SRGAN is initialized with an image of low resolution. This approach provides a better point of reference for the generation of high-resolution images as such the final output is enhanced.

To guarantee that the generated high-resolution images are photo-realistic and at the same time have high perceptual quality, SRGAN employs three types of loss functions for the training of the network. As shown in Eq. (2), the L1 (Mean Absolute Error) or the L2 (Mean Square Error) loss functions are employed to minimize the pixel-wise difference between the reconstructed super-resolved image and the ground truth image. This step allows each of the pixels in the generated image to correspond with a pixel in the high-resolution image.

$$l_{MSE}^{SR} = \frac{1}{r^2 HW} \sum_{x=1}^{rW} \sum_{y=1}^{rH} \left(I_{x,y}^{GT} - G\left(I^{LR} \right) \right)^2 \quad \textbf{(2)}$$

I^{GT} and $G\left(I^{LR}\right)$ represent the ground truth high-resolution image and generated high-resolution image from low-resolution input using the generator G, respectively. H and W are the height and width of the ground truth image and r is the upscaling factor. This pixel-wise loss ensures that each pixel in the generated image closely matches the corresponding pixel in the reference high-resolution image.

Beyond pixel-wise accuracy, SRGAN targets improving the perceptual quality of generated images. To achieve this the model uses VGG loss and adversarial. The VGG loss uses a pre-trained VGG architecture to extract high-level features and textures to produce visually better results [58]. It measures the similarity between the feature maps of the generated image and the ground truth, as defined in Eq. (3):

$$l_{VGG}^{SR} = \sum_{k \in layers} \frac{1}{H_k W_k} \sum_{x=1}^{W_k} \sum_{y=1}^{H_k} \left\| \phi_k \left(I^{HR} \right)_{x,y} - \phi_k \left(G\left(I^{LR} \right) \right)_{x,y} \right\|^2 \quad \textbf{(3)}$$

ϕ_k denotes the feature maps extracted from layer k of the VGG Network, I^{HR} is the ground truth high-resolution image, and $G\left(I^{LR}\right)$ is the generated image. H_k and W_k are the height and width of feature maps at layer k. The VGG loss guides the generator to produce images with better textures and more realistic features by focusing on higher-level abstractions rather than just pixel accuracy.

Additionally, SRGAN uses adversarial loss to force the generator to generate images that are as realistic as high-resolution images. The adversarial loss is defined with the help of a discriminator network D that aims at distinguishing between real and fake images generated by the generator. This adversarial training makes the generator to come up with more realistic images [45].

To improve the performance of the network, ESRGAN [50] made a number of changes: Firstly, to expand the learning capability of the network and to ease the training process, the basic residual blocks were replaced with complex Residual-in-Residual Dense Blocks (RRDB). This modification was important as it helped in better feature representation and

training as the residual blocks are densely connected. Further, to enhance the training process and the quality of the generated images, all the batch normalization layers were eliminated from the network. This removal was beneficial in avoiding the introduction of artifacts that batch normalization can sometimes bring hence improving the training process. Secondly, there were major enhancements to the discriminator part of the network.

Compared to the prior models, the discriminator adopted the Relativistic average GAN (RaGAN) loss [50]. This approach alters the discriminator's way of assessing images, not only deciding whether an image is real or fake but also the degree of realism of generated images to real ones. This relativistic perspective gives more informative feedback, therefore improving the discriminator's capacity to direct the generator toward generating better images. All these modifications combined and contributed to the improvement of the performance where RealESRGAN surpassed SRGAN by providing more realistic images with higher resolution and better texture [55]. The main new feature of the RealESRGAN model is the use of higher-order degradation, which applies random first-order degradation to create more realistic degradations. This approach enables the model to perform well in a greater number of image degradation scenarios, thus making it more practical. While the overall network structure of RealESRGAN is highly similar to that of SRGAN, there is a major improvement in the discriminator network [55].

Unlike other works that use a convolutional network to estimate the likelihood of the input images being real, RealESRGAN employs the UNet. The use of the UNet architecture is a major improvement as it captures more spatial details within the images, thus the discriminator can give more detailed feedback. This improved feedback is important in the enhancement of the parameters of the generator network. By including these changes, RealESRGAN performs better than other models, providing better directions for the generator and therefore improving the image restoration and super-resolution quality [55].

2.2. Evaluation Metrics

By applying super-resolution methods, a predicted image is generated for each of the high-quality images in the test image dataset. Different metrics are used to evaluate the quality and precision of super-resolution algorithms. These metrics are generally categorized into classical and deep learning-based approaches. Classical metrics include Mean Squared Error (MSE), Root Mean Squared Error (RMSE), Peak Signal-to-Noise Ratio (PSNR), and Structural Similarity Index (SSIM). MSE calculates the average squared difference between pixels of the restored and original images, offering simplicity but often poor correlation with human perception. RMSE, a scaled version of MSE, measures error more intuitively, while PSNR assesses signal-to-noise ratio in the reconstructed image, though both metrics lack strong alignment with human visual assessment. SSIM, in contrast, evaluates structural similarity based on luminance, contrast, and structure, making it more suitable for complex structural comparisons [59].

Advanced metrics leverage deep learning to capture perceptual similarity better. For example, Learned Perceptual Image Patch Similarity (LPIPS) uses deep feature extraction to align more closely with human perception but requires pre-trained networks. Fréchet Inception Distance (FID) compares feature distributions to evaluate the similarity between generated and

real images, focusing on quality and realistic appearance. Inception Score (IS) measures the diversity and quality of images generated by GANs, assessing conditional label distribution. Finally, the Multi-Scale Structural Similarity Index (MS-SSIM) extends SSIM to multiple scales, useful in perceptual assessments requiring scaling. Each metric has strengths and weaknesses, making the best choice dependent on the specific goals and requirements of the application [59].

In this study, MSE, RMSE, and PSNR are used as classical metrics that are among the most widely used methods due to the high speed and ease of calculation. The MSE is computed from Eq. (2) and RMSE is the square root of MSE. The value of PSNR is also calculated using Eq. (4).

$$PSNR = 20\log_{10}\left(MAX_{I}\right) - 10\log_{10}\left(MSE\right) \quad \textbf{(4)}$$

Where MAX_I refers to the maximum value among the red, green, and blue components for an RGB color image (255 for an 8-bit RGB image).

In addition to the classic metrics, we also use the LPIPS. For the network training and calculation of this metric, we use lpips library in Python. We first train the model using the training dataset introduced in the results section. LPIPS evaluates the distance between image patches and a higher value means more difference.

2.3. Pore Network Extraction

In pore network modeling, the simplification of pores and throats to spheres and tubes aids in the modeling of single-phase and multi-phase flow with less computational intensity. Different approaches can be used to extract pore network information from images. One of the most popular methods is the Maximal Ball Algorithm, which was described by Silin and Patzek [60]. This has been embraced by researchers because it is so effective in identifying the main themes in the data. But it is time-consuming and the results usually show more throats connected to the pores than in reality. To overcome this problem, Dong and Blunt [29] proposed a two-step algorithm which was an improvement over the initial method and gave a better estimation. Besides these improvements, Sheppard et al. [61] introduced a new extraction technique for pore networks using watershed segmentation. This method was developed to provide a more accurate determination of the pore network structure. The same watershed segmentation technique was later applied by Rabbani et al. [62] on a sandstone sample with low porosity proving the versatility of the technique. Agaesse et al. [63] further expanded on this approach to model flow in the gas diffusion layer of proton exchange membrane fuel cells in a number of applications. On these achievements, Gostick [64] proposed improvements to the watershed segmentation method, which was an over-segmentation technique called SNOW. This was done by flattening some of the peaks in the distance transform; this made the segmentation better for both high and low-porosity rocks.

For extracting pore network data, we use the Snow algorithm which is available in a Python library known as PoreSpy. PoreSpy is a suite of image processing algorithms that is aimed at extracting information from 3D images of porous media that are usually obtained from X-ray tomography. While there are many generic image analysis tools that are available in the market like Skimage and Scipy. In the case of NDimage in the Python environment, ImageJ, and MatLab's Image Processing Toolbox, these may often necessitate the writing of elaborate

scripts or macros to accomplish tasks particular to porous media analysis. Compared to the general purpose tools, PoreSpy is more specialized and allows for more efficient extraction of pore network data from 3D images.

2.4. Flow Calculation

The nature of porous structures makes it very difficult to accurately use conventional fluid dynamics equations such as Navier Stokes equations. These equations while basic in defining the flow of fluids become less useful when analyzing the complex geometry of porous media. To simplify the analysis, the pores and throats in these media are often replaced by simpler shapes such as spheres and tubes which significantly reduces the computational load. As clearly shown by the Hagen–Poiseuille equation (Eq. (5)), there is a direct correlation between the permeability of the fluid (G), pressure drop (ΔP), and flow rate (q):

$$q = G\,\Delta P \tag{5}$$

The fluid permeability for the movement of fluid inside a tube is calculated using Eq. (6) based of viscosity of fluid (μ) and structural property of tube such as length (L) and radius (r):

$$G = \frac{\pi r^4}{\mu L} \tag{6}$$

For each i-th pore, the mass balance is written as Eq. (7) (z represents the number of pores connected to the i-th pore):

$$\sum_{j=1}^{z} q_{ij} = 0 \tag{7}$$

The amount of flow in the throat ij which connects pore j to pore i is calculated as Eq. (8) for a two-phase flow (the single-phase flow equation is the same, but the value of capillary pressure is zero):

$$q_{ij} = G_{ij}\left(P_i - P_j + P_{c,ij}\right) \tag{8}$$

The combination of Eq. (7) and Eq. (8) results in Eq. (9).

$$\sum_{j=1}^{z} G_{ij}\left(P_i - P_j + P_{c,ij}\right) = 0 \tag{9}$$

By applying the constant pressure boundary conditions on the pores at the inlet and outlet of the network and solving the linear equations, the pressure in each pore and the flow in each throat are obtained.

2.5. Preparing Dataset and Experimental Settings

We use images of 4 different rock samples in our work. Table 1 represents more detail of 4 rock samples and Fig. 1 shows some examples of these datasets. In each case, four sample images from different sections are provided to demonstrate the diversity of images.

The first rock sample is chosen for upscaling work because of its multi-scale nature. As shown in Fig. 2, the pore size distribution of this sandstone is bimodal. This characteristic makes the dataset particularly suitable for the objectives of the current study because it enables a study of the various pore scales and their impact. Other rock samples are used to train the RealESRGAN model to create a variety of inputs in the model training process.

To evaluate the pattern recognition method and to be able to reconstruct high-resolution images, we need low-resolution images of the rock sample. To this end, we employ a downsampling strategy. The first principle of downsampling is to reduce the image resolution and pixel number of the image. This process entails choosing a value that represents the new pixel used to replace a set of original pixels. In other words, downsampling is a process of condensing information from several pixels into one pixel; thus, making the image simple but retaining some features. In the present paper, we develop a synthetic dataset that contains images with different degrees of downsampling, namely, 2, 4, 8, 16, and 32.

For example, when the dimensions are scaled down by a factor of 2, each new voxel corresponds to 8 of the original voxels. Before going to the binarization step where the image is converted to black and white, the pixel in the grayscale image has a value of 0-255. To decide the value of each new pixel we calculate the average value of the group of 8 original pixels corresponding to the new pixel.

Fig. 3 shows the results of two different downsampling schemes with a reduction factor of 2. Based on the results of the extraction method, it can be seen that it is better to use an image with the original size for downsampling as shown in Fig. 3(b). Using an image with a smaller size causes unreasonable results due to different settings in the extraction process. Therefore, the method that keeps the size of the images is used, instead of replacing one pixel with, for example, 8 pixels in downsampling with a factor of 2, the pixels remain in the image and only the new pixel value is replaced for the first 8 pixels.

After generating the synthetic images, each image is then converted to a binary format. Fig. 4 presents examples of binary images at all the scales which have been described above. From the images, as shown in Fig. 4, it can be seen that when the resolution of the images is low then there is a lot of detailed information that is lost. The decrease in image resolution entails loss of more detail and this affects the precision of network extraction methods and the generated network.

As stated, when training the model, we require a number of images in various rock samples. To this end, 4 datasets in Table 1 have been employed. One of the issues with these images is the different dimensions, also, given the fact that the increase in the size of the images results in the expansion of time needed to train the model and generate artificial images in GAN [68]. Thus, the selection of an appropriate size that is small enough to be used between the datasets and large enough to represent porous media is critical. Further, this size should be suitable for the creation of images of low resolution as it is intended. From the results obtained in the results section and since size 16 has been selected as the scale factor, the selected size should be able to be downsampled up to 16 times. After checking the data, size 96 is chosen as the desired size, so it is necessary to transfer the initial images to a modified size. Because of the initial size of the images, it is impossible to reduce all the images to the same size, unless we crop the

borders of the images until they get to the closest to the modified size we want which is given for each dataset in Table 2.

In Fig. 5, we provide an example of image modification for each dataset. Each high-resolution image and its desired downsampled image is converted to some new image with a specific size. After upscaling low-resolution test images with the help of the trained model, the generated high-resolution images will be combined to obtain the base high-resolution image as the result of the model. Evaluation metrics are then used to evaluate these outputs.

3. Results and Discussion

3.1. Determining the Downsampling Factor

To study the effect of image resolution on the results of the network analysis, we used downsampled images to extract relevant network data and subsequently construct a pore network model. Fig. 6 shows the effect of different resolutions on permeability in single-phase flow. As shown in Fig. 6, there is a clear trend: the reduction of resolution which in turn means that the smaller pores and throats are excluded from the network, causes a decrease in the porosity and permeability. This is because as image resolution decreases, some of the details within the pore structure are not captured, especially the flow pathways which are important in determining the permeability of the material. Therefore, the removal of these details in the network simplification results in the reduction of the flow and, consequently, lower permeability values. Hence, it is important to comprehend and choose the right resolution when modeling and simulating the fluid flow characteristics in porous media.

For a pore not to be seen in an image, the size of the pixels in the image should be at least twice the size of the pore. When this condition is met, the pore is not considered in the extraction process and hence is not included in the final network. As shown in Fig. 2, the entrance of the pores and throats are usually between 3 to 12 μm in size. This is why even if the pixel size is increased to double these pore sizes, the impact on porosity and permeability is relatively small. But when the resolution is reduced beyond this value, the effects are much higher, and the porosity and permeability are deteriorated to a certain extent. Porosity does not reduce to zero even though the resolution is lowered, because some of the pores are still discernible. However, as the resolution continues to decrease, the pores that connect various pore clusters are eliminated which leads to a significant decrease in permeability to zero value.

As pointed out earlier, and as seen in Fig. 2, at higher pixel sizes, the small pores are almost invisible and one is left with the impression of a large pore rather than a network of small pores. This is shown in Fig. 7 in terms of the modeled pore network for the base images and the downsampled images by a factor of 16. Hence, in these downsampled images, it is crucial to recognize the pattern of these smaller pores and reconstruct the images such that the true characteristics of the pore network are not lost. Table 3 and Table 4 compare network and flow parameters for the original and downsampled network.

3.2. Model Modification

We are going to present our method to address the discussed issue. We formulated the problem as one of super-resolution tasks and used RealESRGAN [55] as our selected super-resolution model. However, the original RealESRGAN has been developed to support only 2x and 4x super-resolution which is not enough for our purpose [69]. The aim of our work is to

create a model that could upsample the input image by a factor of 16. To achieve this, we adjusted the base ESRGAN module in the generator component of the model to increase its capacity to deal with this increased scale factor. Fig. 8 shows the multi-stage enhancement process employed by the RealESRGAN model to achieve a 16x super-resolution. The model, originally designed for 4x upscaling, is applied sequentially in two stages. In the first stage, the low-resolution input image undergoes a 4x super-resolution process, producing an intermediate image with improved resolution and restored details. This intermediate image then serves as the input for the second application of the model, further enhancing the resolution by another 4x, resulting in a final output with a total 16x improvement in resolution. This approach leverages the model's ability to effectively upscale images while preserving fine details, as demonstrated by the progressive refinement observed in the intermediate and final outputs. The two-stage process ensures that finer structures and textures are reconstructed incrementally, avoiding artifacts that could arise from a single, large-scale transformation. Such a methodology is particularly effective for applications in porous media analysis, where retaining the intricate details of pore structures is crucial for accurate modeling and analysis

3.3. Results of Model Training

The modified dataset we have used for our experiments contains 17636 images. From this dataset, we used 10,724 images for training and the rest of the images were used for testing. To speed up the training, we fine-tuned the weights corresponding to the 4x scale factor for the parameters that were present in our extended model. The training of the model was done using the Adam optimizer with $\beta 1 = 0.9$ and $\beta 2 = 0.99$. We trained the model for more than 150,000 iterations with the help of Nvidia GeForce RTX 3090 GPU which took almost 44 hours. During the training, the batch size was set to 8 to enhance the processing rate. Fig. 9 shows the calculated loss function value for all images after 150,000 iterations.

As shown in Fig. 9, after 50,000 iterations, there is no significant change in the amount of loss function. In addition, continuing these iterations can lead to overfitting of the model on the current data. Therefore, by accepting the data obtained after 50,000 attempts, we use the generated results for the pore network modeling.

Fig. 10 to Fig. 13 show some examples of the generated image along with the original and the downsampled image for each dataset. As shown, the difference between the images is very small and in some cases, it cannot be distinguished. So, it is necessary to use evaluation metrics to discover the difference between generated and original high-resolution images.

3.4. Evaluation of Results

As mentioned, 4 different criteria are used to evaluate the accuracy of the model. Fig. 14 shows a comparison between different evaluation metrics. The low values of MSE and RMSE indicate more similarity between images, so as shown in Fig. 14, our super-resolution algorithm has been able to bring the generated images closer to the real ones in terms of these two metrics. In addition, the higher PSNR indicates more similarity, which also confirms the proper performance of the model.

We discussed that the classical criteria cannot understand human perception very well. The LPIPS can check this issue to a good extent. By looking at the results in Fig. 14 and comparing

them with the results of Jo et, al. [70], we realize that according to the LPIPS metric, the images are produced with proper accuracy. Lower values of LPIPS show more similarity between images. Jo et al. [70] have been able to produce images with a scale factor of 16, which compared to the real images, had an average LPIPs value of 0.25 in the best case. As shown in Fig. 14, except for one of our datasets, we have been able to get better results than this paper. However, in the Doddington sample, we have also a good result, which is comparable to the results of the mentioned article.

We can see in Fig. 14 that the low-quality images and generated high-resolution images have less difference from each other. While in LPIPS charts there is a greater difference between these images. This issue shows that the classical metrics cannot be a suitable metric in such problems and may lead to unreliable results and false image quality enhancement.

3.5. Final Pore Network Model

The last process is to use all the images produced by RealESRGAN to build the pore network model. We use high-resolution generated images in multi-scale sandstone dataset to build our pore network model. It is believed that by incorporating the high-quality image enhancement from the RealESRGAN, the pore network model will have improved accuracy and efficiency in portraying the pore structures. Fig. 15 shows the network model obtained from real images and generated images. Table 3 and Table 4 compare network and flow parameters for the original and generated network. It is clear from these tables that the number of pores and throats has increased, but the increase in the pores and throats volume in the generated network is less than the increase in their number. This shows that the model tends to generate some pores and throats with smaller sizes. However, this issue does not have much effect on the final result and the flow properties of the network.

3.6. Discussion

In this article, a new method used in the modern science of computer engineering called RealESRGAN is used. Super-resolution techniques can be applied in different fields of petroleum engineering to improve the quality of images. These applications are; enhancing the resolution of seismic data for better interpretation of subsurface structures, reconstructing well log data and core sample images for more accurate reservoir property analysis, enhancing the quality of satellite and remote sensing images for modeling exploratory regions, and increasing the resolution of Synthetic Aperture Radar (SAR) images for monitoring surface changes and geological analysis [71]. Such techniques help in improving the accuracy of the reservoir evaluation and in decision-making in exploration. One of its applications that is mentioned in this paper is related to increasing the quality of porous media images. The lack of high-quality images often causes the flow properties obtained from the pore network model to not match the laboratory results in some porous media. To find such criteria we studied different porous media and we found that in a multi-scale sandstone, happened by studying a multi-scale sandstone sample in section 3.1. The results showed that in this network, by reducing the resolution, some pores with a size smaller than the specified size are removed, which, as a result, reduces the permeability of the pore network model. This shows that this dataset is a suitable option for our work.

The purpose of our work is to use the original low-quality images and increase their quality to recover the lost details. For this purpose, we used the RealESRGAN method. RealESRGAN is designed based on ESRGAN with the Residual-in-Residual Dense block and the Perceptual Loss, and it can generate images with more realistic and sharper images than the original method. These features and the stability during training make this choice suitable for petroleum engineering applications where high-quality images are required. Because of the nature of the problem a sample that is sensitive to the resolution reduction is required and thus a multiscale sandstone sample was included. Because the size of the pores and throats in the sample is bimodal, the loss of detail in the images used to construct the pore network model was apparent and details had to be recovered in this sample. To train the model, using only the images of a dataset can cause problems such as overfitting. Therefore, we also use three other datasets in the model training process. To evaluate the results of the model, different classical and new evaluation metrics are used. The results show that in such problems, the use of classical metrics because the criteria only measure the pixel similarity between the images, can confirm the false quality of the images. The new metrics such as Lpips used in this research can better distinguish the difference between the images. So, using the LPIPS we can evaluate the result of the model. Finally, the pore network model is constructed using the generated high-resolution images from the model. The comparison between the generated model and the original network shows that the obtained model is reasonably close to the real model, although there are also minor differences that did not have much effect on the flow parameters of the model.

As mentioned in the introduction section, different super-resolution methods such as Transformer-based SR models and Diffusion models are introduced. The void of these methods can be felt in the study of porous media, especially in increasing the quality of images and recovering the lost details. As a suggestion for the next works, the application of these methods can be used to increase the quality of porous media images.

In this research, we use 16 as an upscaling factor. One of the things that can be investigated in the future is the use of different scale factors in the process of training the model and comparing the results. The use of different scale factors requires retraining the model, which makes it difficult due to the long training time of the model. To speed up the training process of the model, we can use other methods such as TPUs (Tensor Processing Units) and FPGAs (Field-Programmable Gate Arrays) [72]. The use of these methods increases the speed of the model, which allows us to work with a larger dataset.

TPUs are highly optimized for machine learning tasks, especially deep learning, as they excel in performing fast matrix operations with high efficiency. While FPGAs offer flexibility by allowing custom designs tailored to specific tasks, they tend to be faster for highly specialized applications but require more effort in design and optimization. Overall, TPUs generally lead in speed for deep learning, while GPUs are better for general-purpose parallel tasks, and FPGAs shine in custom, specialized applications [72].

4. Conclusion and Recommendation

To improve the quality of the images of the pore network, we employed RealESRGAN. The conventional GAN techniques are employed to create fake images and cannot enhance the resolution of the low-quality images. Thus, we used this model that has the ability to perform

super-resolution. First, a study was conducted to demonstrate that the selected dataset of a multi-scale sandstone contained suitable images. We assessed the impact of reducing the resolution, which revealed that in this dataset, characterized by a bimodal pore size distribution, resolution reduction, decreases porosity and permeability due to the loss of smaller pores. We used 3 other datasets to reach the dataset for training the model. Finally, using the RealESRGAN method, we were able to obtain synthetic images that look almost real. Different metrics were used to evaluate the accuracy of the model, and the results show that the LPIPS is a more suitable metric to evaluate the results of the model.

To further test the model on other rock samples, it is recommended that the model be applied to broader datasets, including those that it has not encountered before. This will determine whether it can accurately replicate the results or improve the quality of existing images. Additionally, this model can be employed in the construction of multi-scale networks to model detailed parts within large domain networks.

References

1. Muther, T., Qureshi, H.A., Syed, F.I., et al. “Unconventional hydrocarbon resources: geological statistics, petrophysical characterization, and field development strategies”, *Journal of Petroleum Exploration and Production Technology*, **12**(6), pp.1463-1488 (2022). https://doi.org/10.1007/s13202-021-01404-x
2. Hui, G., Chen, Z., Wang, Y., et al. “An integrated machine learning-based approach to identifying controlling factors of unconventional shale productivity”, *Energy*, **266**, p.126512 (2023). https://doi.org/10.1016/j.energy.2022.126512
3. Tahmasebi, P., and Kamrava, S. “Rapid multiscale modeling of flow in porous media”, *Physical Review E*, **98**(5), p.052901 (2018). https://doi.org/10.1103/PhysRevE.98.052901
4. Yang, Y., Li, Y., Yao, J., et al. “Dynamic pore-scale dissolution by CO2-saturated brine in carbonates: Impact of homogeneous versus fractured versus vuggy pore structure”, *Water Resources Research*, **56**(4), p.e2019WR026112 (2020). https://doi.org/10.1029/2019WR026112
5. Zhang, J., Zhang, N., Sun, X., et al. “Pore-scale investigation on methane hydrate formation and plugging under gas–water flow conditions in a micromodel”, *Fuel*, **333**, p.126312 (2023). https://doi.org/10.1016/j.fuel.2022.126312
6. Scheibe, T.D., Perkins, W.A., Richmond, M.C., et al. “Pore-scale and multiscale numerical simulation of flow and transport in a laboratory-scale column”, *Water Resources Research*, **51**(2), pp.1023-1035 (2015). https://doi.org/10.1002/2014WR015959
7. de Vries, E.T., Raoof, A., and van Genuchten, M.T. “Multiscale modelling of dual-porosity porous media; a computational pore-scale study for flow and solute transport”, *Advances in water resources*, **105**, pp.82-95 (2017). https://doi.org/10.1016/j.advwatres.2017.04.013
8. Wu, Y., Tahmasebi, P., Lin, C., et al. “Effects of micropores on geometric, topological and transport properties of pore systems for low-permeability porous media”, *Journal of Hydrology*, **575**, pp.327-342 (2019). https://doi.org/10.1016/j.jhydrol.2019.05.014
9. Shams, R., Masihi, M., Boozarjomehry, R.B., et al. “A hybrid of statistical and conditional generative adversarial neural network approaches for reconstruction of 3D porous media (ST-CGAN)”, *Advances in Water Resources*, **158**, p.104064 (2021). https://doi.org/10.1016/j.advwatres.2021.104064
10. Diamond, S. “Mercury porosimetry: An inappropriate method for the measurement of pore size distributions in cement-based materials”, *Cement and concrete research*, **30**(10), pp.1517-1525 (2000). https://doi.org/10.1016/S0008-8846(00)00370-7
11. Čapek, P., Veselý, M., and Hejtmánek, V. “On the measurement of transport parameters of porous solids in permeation and Wicke–Kallenbach cells”, *Chemical Engineering Science*, **118**, pp.192-207 (2014). https://doi.org/10.1016/j.ces.2014.07.039
12. Mostaghimi, P., Blunt, M.J., and Bijeljic, B. “Computations of absolute permeability on micro-CT images”, *Mathematical Geosciences*, **45**, pp.103-125 (2013). https://doi.org/10.1007/s11004-012-9431-4
13. Duwig, C., Delmas, P., Müller, K., et al. “Quantifying fluorescent tracer distribution in allophanic soils to image solute transport”, *European Journal of Soil Science*, **59**(1), pp.94-102 (2008). https://doi.org/10.1111/j.1365-2389.2007.00970.x
14. Dikinya, O., Hinz, C., and Aylmore, G. “Decrease in hydraulic conductivity and particle release associated with self-filtration in saturated soil columns”, *Geoderma*, **146**(1-2), pp.192-200 (20018). https://doi.org/10.1016/j.geoderma.2008.05.014
15. Zeinijahromi, A., Farajzadeh, R., Bruining, J.H. et al. “Effect of fines migration on oil–water relative permeability during two-phase flow in porous media”, *Fuel*, *176*, pp.222-236 (2016). https://doi.org/10.1016/j.fuel.2016.02.066

16. Gerke, K.M., Vasilyev, R.V., Khirevich, S., et al. “Finite-difference method Stokes solver (FDMSS) for 3D pore geometries: Software development, validation and case studies”, *Computers & geosciences*, **114**, pp.41-58 (2018).
https://doi.org/10.1016/j.cageo.2018.01.005
17. Blunt, M.J., Bijeljic, B., Dong, H. “Pore-scale imaging and modelling”, *Advances in Water resources*, **51**, pp.197-216 (2013).
https://doi.org/10.1016/j.advwatres.2012.03.003
18. Carman, P.C. “Permeability of saturated sands, soils and clays”, *The Journal of Agricultural Science*, **29**(2), pp.262-273 (1939).
19. Nishiyama, N. and Yokoyama, T. “Permeability of porous media: Role of the critical pore size”, *Journal of Geophysical Research: Solid Earth*, **122**(9), pp.6955-6971 (2017).
https://doi.org/10.1002/2016JB013793
20. Xu, P. and Yu, B. “Developing a new form of permeability and Kozeny–Carman constant for homogeneous porous media by means of fractal geometry”, *Advances in water resources*, **31**(1), pp.74-81 (2008).
https://doi.org/10.1016/j.advwatres.2007.06.003
21. Gackiewicz, B., Lamorski, K., Sławiński, C., et al. “An intercomparison of the pore network to the Navier–Stokes modeling approach applied for saturated conductivity estimation from X-ray CT images”, *Scientific reports*, **11**(1), p.5859 (2021).
https://doi.org/10.1038/s41598-021-85325-z
22. Xie, Y., Chen, Z., and Du, Z., “The Construction and Application of a Simplified Pore Network Model Based on Computerized Tomography”, *Scientia Iranica*, **23**(3), pp.1184-1194 (2016).
https://doi.org/10.24200/sci.2016.3888
23. Evans, L.M., Sözümert, E., Keenan, B.E., et al. “A Review of image-based simulation applications in high-value manufacturing”, *Archives of Computational Methods in Engineering*, pp.1-58 (2023).
https://doi.org/10.1007/s11831-022-09836-2
24. Haggerty, R. and Gorelick, S.M. “Multiple-rate mass transfer for modeling diffusion and surface reactions in media with pore-scale heterogeneity”, *Water Resources Research*, **31**(10), pp.2383-2400 (1995).
https://doi.org/10.1029/95WR10583
25. Carrera, J., Sánchez-Vila, X., Benet, I., et al. “On matrix diffusion: formulations, solution methods and qualitative effects”, *Hydrogeology Journal*, **6**, pp.178-190 (1998).
https://doi.org/10.1007/s100400050143
26. Gouze, P., Melean, Y., Le Borgne, T., et al. “Non-Fickian dispersion in porous media explained by heterogeneous microscale matrix diffusion. *Water Resources Research*, **44**(11) (2008).
https://doi.org/10.1029/2007WR006690
27. Shabro, V., Torres-Verdin, C., and Javadpour, F. “Numerical simulation of shale-gas production: from pore-scale modeling of slip-flow, Knudsen diffusion, and Langmuir desorption to reservoir modeling of compressible fluid”, *SPE Unconventional Resources Conference/Gas Technology Symposium*, pp. SPE-144355 (2011).
https://doi.org/10.2118/144355-MS
28. Gjetvaj, F., Russian, A., Gouze, P., et al. “Dual control of flow field heterogeneity and immobile porosity on non-Fickian transport in Berea sandstone”, *Water Resources Research*, *51*(10), pp.8273-8293 (2015).
https://doi.org/10.1002/2015WR017645
29. Dong, H. and Blunt, M.J. “Pore-network extraction from micro-computerized-tomography images”, *Physical Review E—Statistical, Nonlinear, and Soft Matter Physics*, **80**(3), p.036307 (2009).
https://doi.org/10.1103/PhysRevE.80.036307
30. Joekar-Niasar, V. and Hassanizadeh, S.M. “Analysis of fundamentals of two-phase flow in porous media using dynamic pore-network models: a review”, *Critical reviews in environmental science and technology*, **42**(18), pp.1895-1976 (2012).
https://doi.org/10.1080/10643389.2011.574101
31. Liu, Y., Guo, C., Cao, J., et al. “A new resolution enhancement method for sandstone thin-section images using perceptual GAN”, *Journal of Petroleum Science and Engineering*, **195**, p.107921 (2020).
https://doi.org/10.1016/j.petrol.2020.107921

32. Behrenbruch, C.P., Petroudi, S., Bond, S., et al. “Image filtering techniques for medical image post-processing: an overview”, *The British journal of radiology*, **77**(suppl_2), pp.S126-S132 (2004). https://doi.org/10.1259/bjr/17464219
33. Singh, K. and Kapoor, R. “Image enhancement using exposure based sub image histogram equalization”, *Pattern Recognition Letters*, **36**, pp.10-14 (2014). https://doi.org/10.1016/j.patrec.2013.08.024
34. Tang, H., Wu, E.X., Ma, Q.Y., et al. “MRI brain image segmentation by multi-resolution edge detection and region selection”, *Computerized Medical Imaging and Graphics*, **24**(6), pp.349-357 (2000). https://doi.org/10.1016/s0895-6111(00)00037-9
35. Da Wang, Y., Armstrong, R., and Mostaghimi, P. “Super resolution convolutional neural network models for enhancing resolution of rock micro-ct images”, *arXiv preprint arXiv:*1904.07470 (2019). https://doi.org/10.1016/j.petrol.2019.106261
36. Lepcha, D.C., Goyal, B., Dogra, A. et al. “Image super-resolution: A comprehensive review, recent trends, challenges and applications”, *Information Fusion*, **91**, pp.230-260 (2023). https://doi.org/10.1016/j.inffus.2022.10.007
37. Karsanina, M.V., Gerke, K.M., Skvortsova, et al. “Enhancing image resolution of soils by stochastic multiscale image fusion”, *Geoderma*, **314**, pp.138-145 (2018). https://doi.org/10.1016/j.geoderma.2017.10.055
38. Zhao, W., Zhao, S., Li, L., et al. “Sparse deconvolution improves the resolution of live-cell super-resolution fluorescence microscopy”, *Nature biotechnology*, **40**(4), pp.606-617 (2022). https://doi.org/10.1038/s41587-021-01092-2
39. Liu, J., Malekzadeh, M., Mirian, N., et al. “Artificial intelligence-based image enhancement in pet imaging: Noise reduction and resolution enhancement”, *PET clinics*, *16*(4), pp.553-576 (2021). https://doi.org/10.1016/j.cpet.2021.06.005
40. Mohan, A., Dwivedi, R., and Kumar, B., “Image restoration of landslide photographs using SRCNN”, *Recent Trends in Electronics and Communication: Select Proceedings of VCAS 2020*, pp.1249-1259 (2022). https://doi.org/10.1007/978-981-16-2761-3_108
41. Lee, K.M., Lee, P.J., and Bui, T.A. “Edge Detection Cascaded with Simplified WDSR of IR Super Resolution”, *International Conference on System Science and Engineering (ICSSE)*, pp. 378-381 (2021). https://doi.org/10.1109/ICSSE52999.2021.9538439
42. Lin, K. “The performance of single-image super-resolution algorithm: EDSR”, *IEEE international conference on information systems and computer aided education (ICISCAE)*, pp. 964-968 (2022). https://doi.org/10.1109/ICISCAE55891.2022.9927560
43. Rajamohana, S.P., Thamaraiselvi, S., Bibraj, R., et al. “A Review and Analysis of GAN-Based Super-Resolution Approaches for INSAT 3D/3DR Satellite Imagery using Artificial Intelligence: GAN BASED APPROACHES FOR INSAT 3D/3DR SATELLITE IMAGERY USING AI”, *Journal of Scientific & Industrial Research (JSIR*), **83**(6), pp.627-638 (2024). https://doi.org/10.56042/jsir.v83i6.7320
44. Striuk, O. and Kondratenko, Y. “Generative adversarial neural networks and deep learning: successful cases and advanced approaches”, *International Journal of Computing*, **20**(3), pp.339-349 (2021). https://doi.org/10.47839/ijc.20.3.2278
45. Ledig, C., Theis, L., Huszár, F., et al. “Photo-realistic single image super-resolution using a generative adversarial network”, *Proceedings of the IEEE conference on computer vision and pattern recognition*, pp. 4681-4690 (2017). https://doi.org/10.48550/arXiv.1609.04802
46. Lei, Y., Zhu, Z., Qin, Y., et al. “Residual SwinV2 transformer coordinate attention network for image super resolution” *AI Communications*, pp.1-17 (2024). https://doi.org/10.3233/AIC-230340
47. Zhu, Z., Lei, Y., Qin, Y., et al. “IRE: improved image super-resolution based on real-ESRGAN”, *IEEE Access*, **11**, pp.45334-45348 (2023). https://doi.org/10.3390/rs16132312

48. Striuk, O. and Kondratenko, Y. “Implementation of generative adversarial networks in mobile applications for image data enhancement”, *Journal of Mobile Multimedia*, pp.823-838 (2023). https://doi.org/10.13052/jmm1550-4646.1938
49. Striuk, O. and Kondratenko, Y. “Optimization Strategy for Generative Adversarial Networks Design”, *International Journal of Computing*, **22**(3), pp. 292–301 (2023). https://doi.org/10.47839/ijc.22.3.3223
50. Wang, X., Yu, K., Wu, S., et al. “Esrgan: Enhanced super-resolution generative adversarial networks”, *Proceedings of the European conference on computer vision (ECCV) workshops*, pp. 0-0 (2018). https://doi.org/10.48550/arXiv.1809.00219
51. Jiang, K., Wang, Z., Yi, P., et al. “Edge-enhanced GAN for remote sensing image superresolution”, *IEEE Transactions on Geoscience and Remote Sensing*, **57**(8), pp.5799-5812 (2019). https://doi.org/10.1109/TGRS.2019.2902431
52. Gan, W., Zhao, Z., Wang, Y., et al. “UDGAN: A new urban design inspiration approach driven by using generative adversarial networks”, *Journal of Computational Design and Engineering*, **11**(1), pp.305-324 (2024). https://doi.org/10.1093/jcde/qwae014
53. Tu, J., Mei, G., Ma, Z., et al. “SWCGAN: Generative adversarial network combining swin transformer and CNN for remote sensing image super-resolution”, *IEEE Journal of Selected Topics in Applied Earth Observations and Remote Sensing*, **15**, pp.5662-5673 (2022). https://doi.org/10.1109/jstars.2022.3190322
54. Jia, M., Hou, B., Jia, F.C., et al. “Enhancement-mode AlGaN/GaN HEMTs with a semi-wraparound metal-insulator-semiconductor gate”, *International Symposium on Next-Generation Electronics (ISNE)*, pp. 1-3 (2023). https://doi.org/10.1109/ISNE56211.2023.10221606
55. Wang, X., Xie, L., Dong, C., et al. “Realesrgan: Training real-world blind super-resolution with pure synthetic data supplementary material”, *Computer Vision Foundation open access*, **1**(2), p.2 (2022). https://doi.org/10.1109/ICCVW54120.2021.00217
56. Tang, H., Zhu, H., Fei, L., et al. “Low-illumination image enhancement based on deep learning techniques: a brief review”, *Photonics*, p. 198 (2023). https://doi.org/10.3390/photonics10020198
57. Goodfellow, I., Pouget-Abadie, J., Mirza, M., et al. “Generative adversarial nets”, *Advances in neural information processing systems*, **27** (2014). https://doi.org/10.1145/3422622
58. Simonyan, K. and Zisserman, A. “Very deep convolutional networks for large-scale image recognition”, *arXiv preprint arXiv:*1409.1556 (2014). https://doi.org/10.48550/arXiv.1409.1556
59. Arabboev, M., Begmatov, S., Rikhsivoev, M., et al. “A comprehensive review of image super-resolution metrics: classical and AI-based approaches”, *Acta IMEKO*, **13**(1), pp.1-8. https://doi.org/10.21014/actaimeko.v13i1.1679
60. Silin, D. and Patzek, T. “Pore space morphology analysis using maximal inscribed spheres”, *Physica A: Statistical mechanics and its applications*, **371**(2), pp.336-360 (2006). https://doi.org/10.1016/j.physa.2006.04.048
61. Sheppard, A.P., Sok, R.M., and Averdunk, H. “Improved pore network extraction methods”, *International Symposium of the Society of Core Analysts*, pp. 1-11 (2005).
62. Rabbani, A., Jamshidi, S., and Salehi, S. “An automated simple algorithm for realistic pore network extraction from micro-tomography images”, *Journal of Petroleum Science and Engineering*, **123**, pp.164-171 (2014). https://doi.org/10.1016/j.petrol.2014.08.020
63. Agaesse, T., Lamibrac, A., Büchi, F.N., et al. “Validation of pore network simulations of ex-situ water distributions in a gas diffusion layer of proton exchange membrane fuel cells with X-ray tomographic images”, *Journal of Power Sources*, **331**, pp.462-474 (2016). https://doi.org/10.1016/j.jpowsour.2016.09.076

64. Gostick, J.T. “Versatile and efficient pore network extraction method using marker-based watershed segmentation”, *Physical Review E,* **96**(2), p.023307 (2017).
https://doi.org/10.1103/PhysRevE.96.023307
65. Mohammadmoradi, P., and Kantzas, A. “DyMAS: a direct multi-scale pore-level simulation approach”, *SPE Western Regional Meeting,* p. D031S007R004 (2017).
https://doi.org/10.2118/185720-MS
66. Neumann, R.F., Barsi-Andreeta, M., Lucas-Oliveira, E., et al. “High accuracy capillary network representation in digital rock reveals permeability scaling functions”, *Scientific reports*, **11**(1), p.11370 (2021).
https://doi.org/10.1038/s41598-021-90090-0
67. Moon, C., Mitchell, S.A., Heath, J.E., et al. “Statistical inference over persistent homology predicts fluid flow in porous media”, *Water Resources Research*, **55**(11), pp.9592-9603 (2019).
https://doi.org/10.1029/2019WR025171
68. Mosser, L., Dubrule, O., and Blunt, M.J. “Reconstruction of three-dimensional porous media using generative adversarial neural networks”, *Physical Review E,* **96**(4), p.043309 (2017).
https://doi.org/10.1103/PhysRevE.96.043309
69. Wang, H., Wu, W., Su, Y., et al. “Image super-resolution using a improved generative adversarial network”, *Conference on Electronics Information and Emergency Communication (ICEIEC),* pp. 312-315 (2019).
https://doi.org/10.110 9/ICEIEC.2019.8784610
70. Jo, Y., Yang, S., and Kim, S.J. “Investigating loss functions for extreme super-resolution”, *IEEE/CVF Conference on Computer Vision and Pattern Recognition Workshops*, pp. 424-425 (2020).
https://doi.org/10.1109/cvprw50498.2020.00220
71. Wu, B., Meng, D., and Zhao, H. “Semi-supervised learning for seismic impedance inversion using generative adversarial networks”, *Remote Sensing*, **13(**5), p.909 (2021)
https://doi.org/10.3390/rs13050909
72. Sipola, T., Alatalo, J., Kokkonen, T., et al. “Artificial intelligence in the IoT era: A review of edge AI hardware and software”, *Conference of Open Innovations Association (FRUCT),* pp. 320-331 (2022).
https://doi.org/10.23919/FRUCT54823.2022.9770931

Biographies

Alireza ElahiKhaledi is a Ph.D. Candidate of Petroleum Engineering at Sharif University of Technology in Tehran. He obtained his undergraduate degree in petroleum engineering in 2017 and his MSc degree in Petroleum Engineering-Drilling Engineering in 2019 both from Sharif University of Technology. Her research interests are Pore Network Modeling and Application of Artificial Intelligence in Petroleum Engineering.

Dr. Saeid Jamshidi is an Associate Professor of Petroleum Engineering in the Department of Chemical and Petroleum Engineering at Sharif University of Technology in Tehran. He obtained his undergraduate degree in petroleum engineering in 2003 from the Petroleum University of Technology (PUT), Ahvaz, Iran, and his MSc degree in Petroleum Engineering-Hydrocarbon Reservoir Engineering in 2005, Department of Chemical & Petroleum Engineering, Sharif University of Technology, Tehran, Iran. He also received his Ph.D. in Petroleum Engineering in 2010 from the Sharif University of Technology. He worked on 'Application of Data Compression and Cellular Development Algorithms in Pore Network Modeling' as his PhD thesis and after that started working as an assistant professor at the Sharif University of Technology. He was promoted to Associate Professor in 2018 at this university and he has performed several student and industrial projects mainly in the field of applications of soft computing in petroleum engineering and developed several software applications for the petroleum industry.

Dr. Mohsen Masihi is a Professor of Petroleum Engineering in the Department of Chemical and Petroleum Engineering at Sharif University of Technology in Tehran. He earned his PhD in Petroleum Engineering from Imperial College London in 2006. His research interests cover various aspects of reservoir engineering, ranging from characterization to pore-scale and field-scale modeling and simulation of conventional and unconventional reservoirs.

Figures

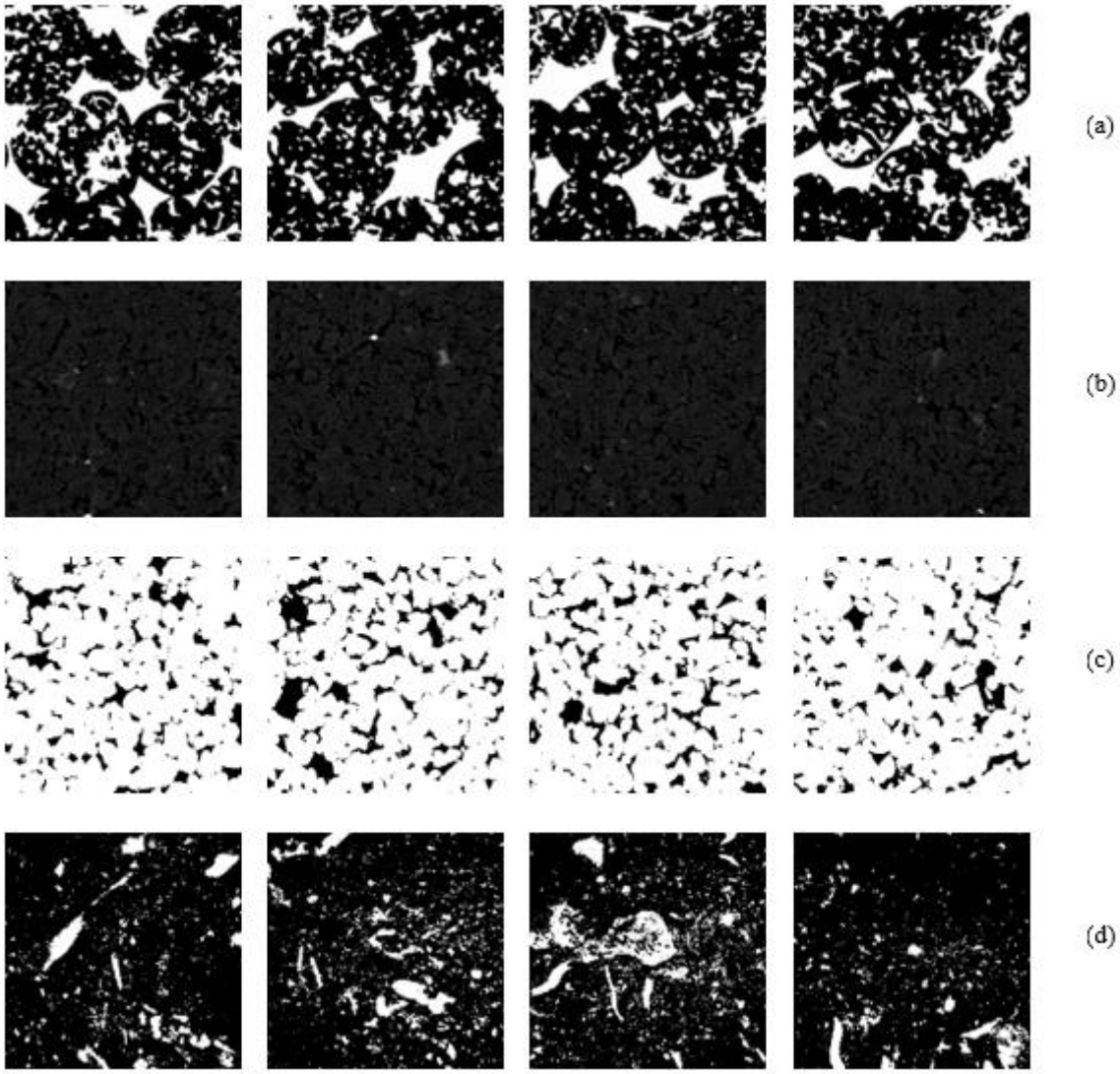

Fig. 1 Sample images for (a) multi-scale sandstone, (b) Brea Sandstone, (c) Doddington sandstone, and (d) tight carbonate

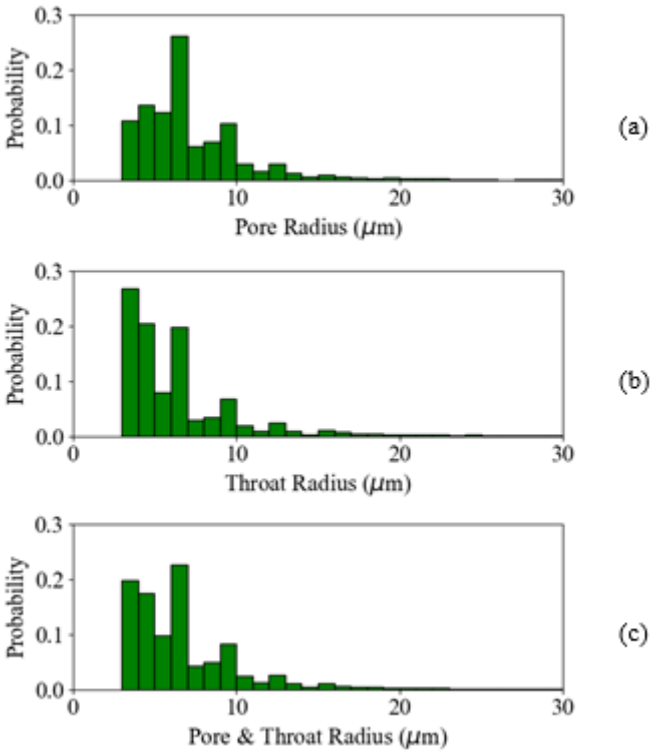

Fig. 2 Probability distribution for (a) pore size, (b) throat size, and (c) sizes of all pores and throats in multi-scale sandstone

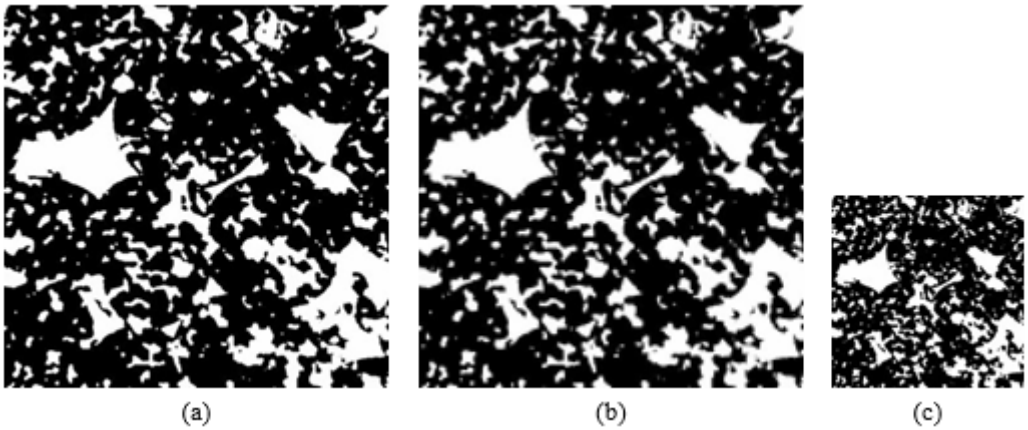

Fig. 3 An example of (a) the original image, (b) a downsampled image with a factor of 4 at the same size as the original, and (c) a downsampled image with a factor of 4 with a reduced size, in multi-scale sandstone

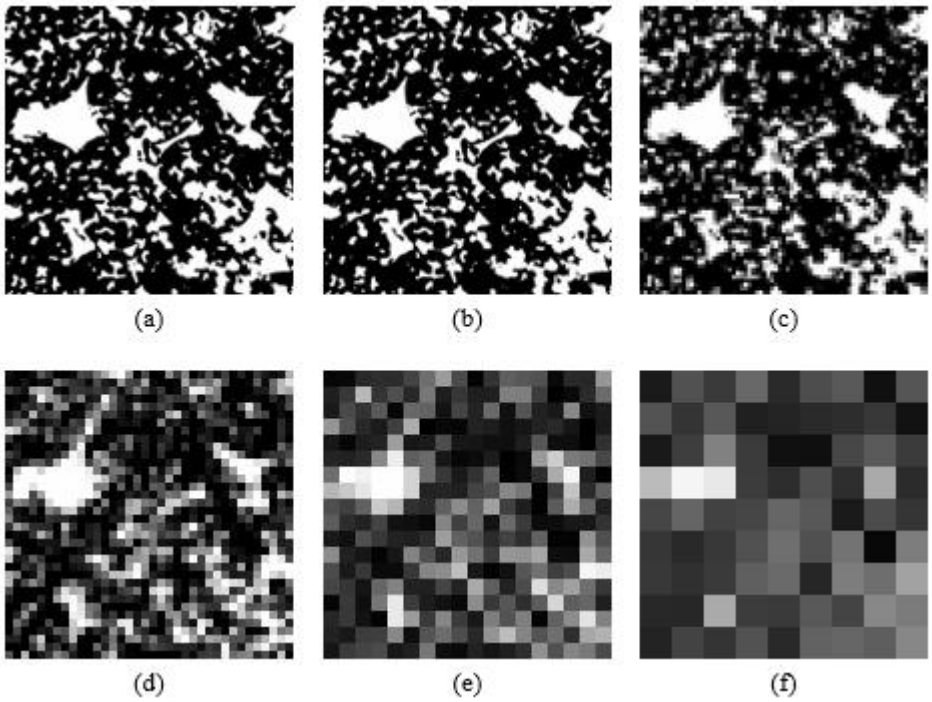

Fig. 4 An example of (a) original image, and synthetic images with (b) 2, (c) 4, (d) 8, (e) 16, (f) 32, times reduction in dimension in multi-scale sandstone

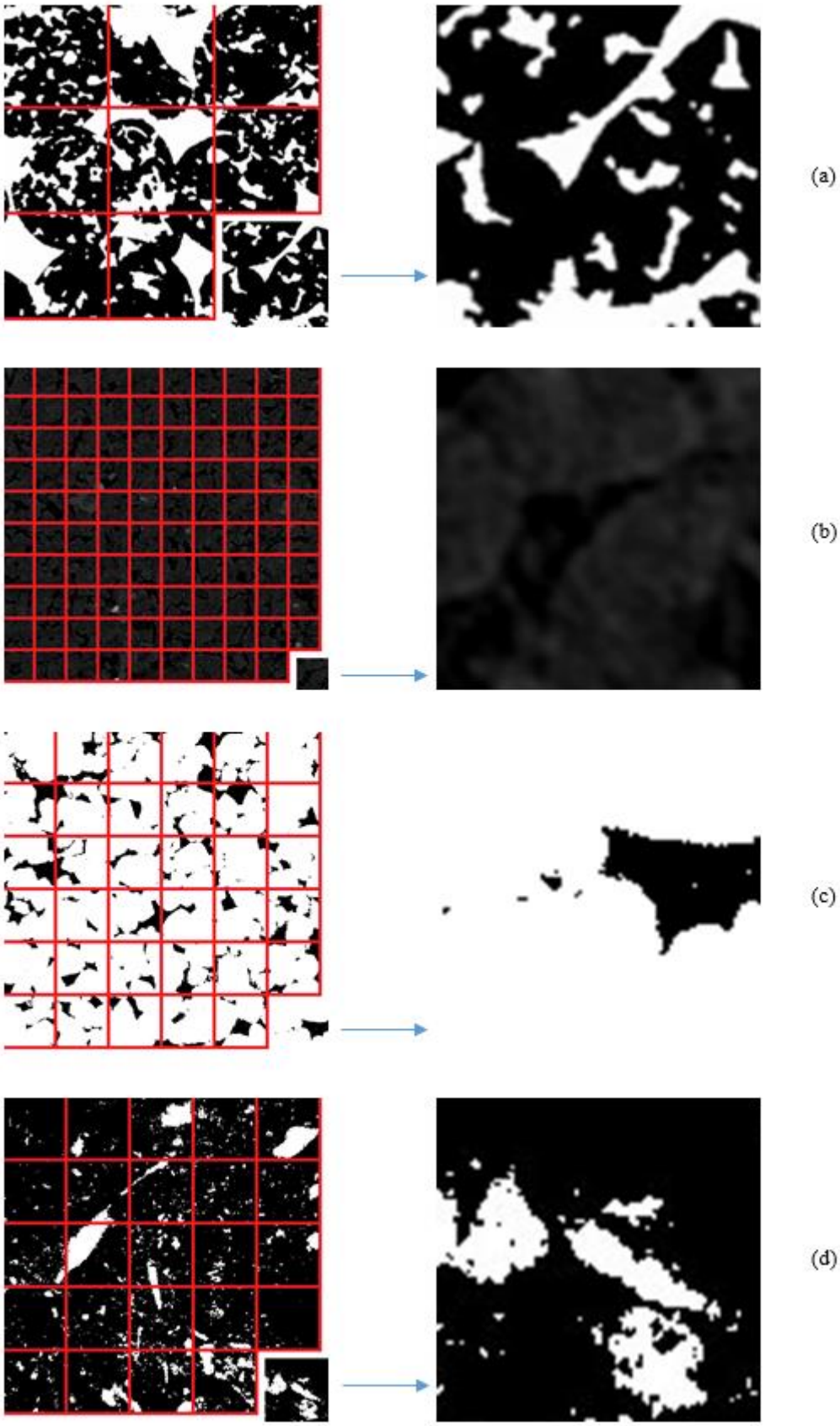

Fig. 5 Example of image modification in (a) multi-scale sandstone, (b) Brea Sandstone, (c) Doddington sandstone, and (d) tight carbonate

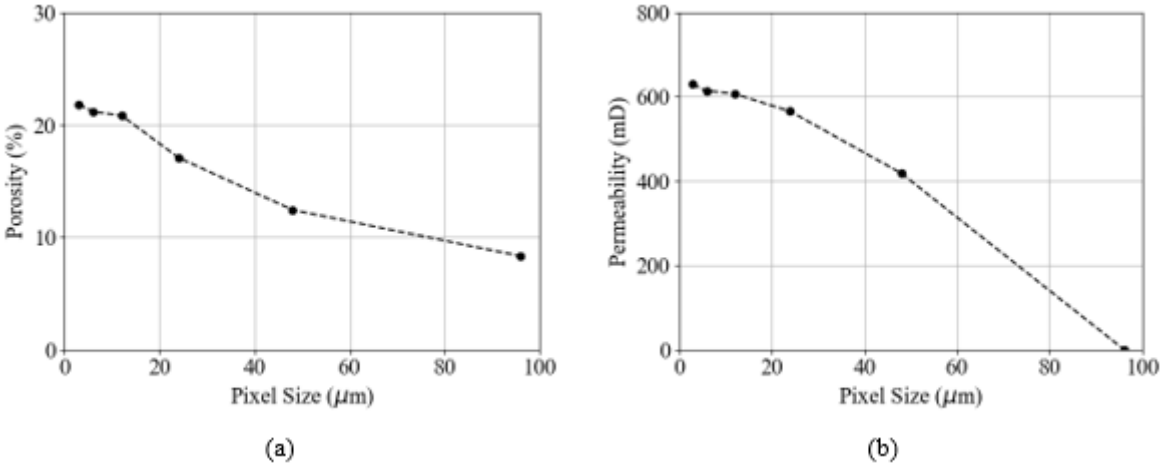

Fig. 6 Effect of resolution on (a) porosity, and (b) single phase permeability, of multi-scale sandstone

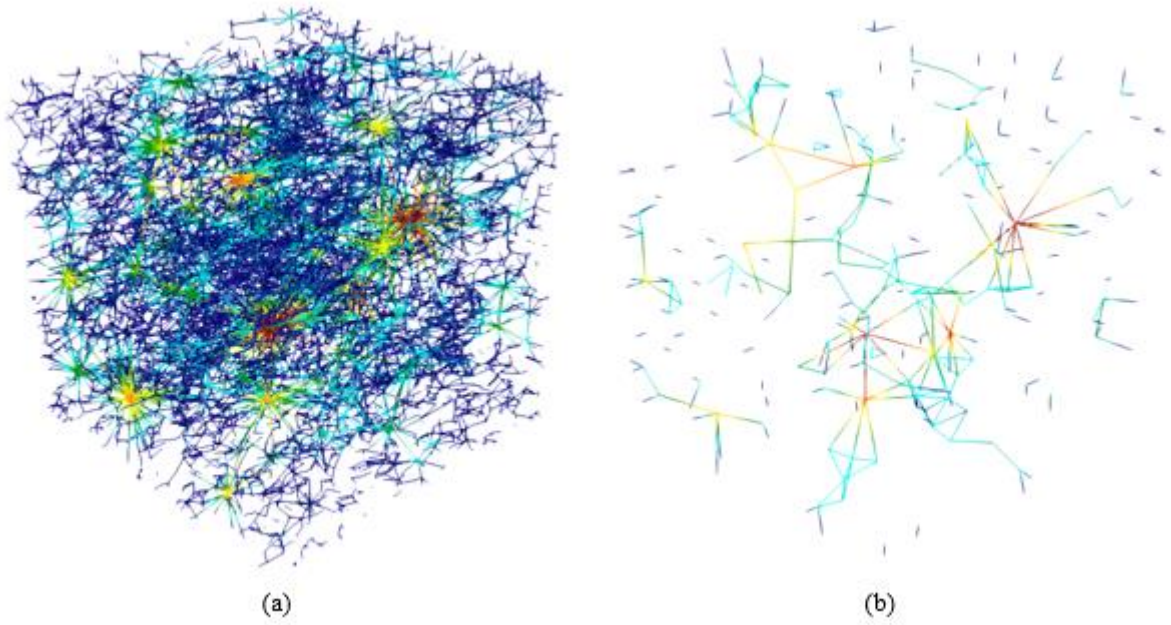

Fig. 7 Pore network model using (a) original images (b) downsampled images by scale factor of 16, in multi-scale sandstone

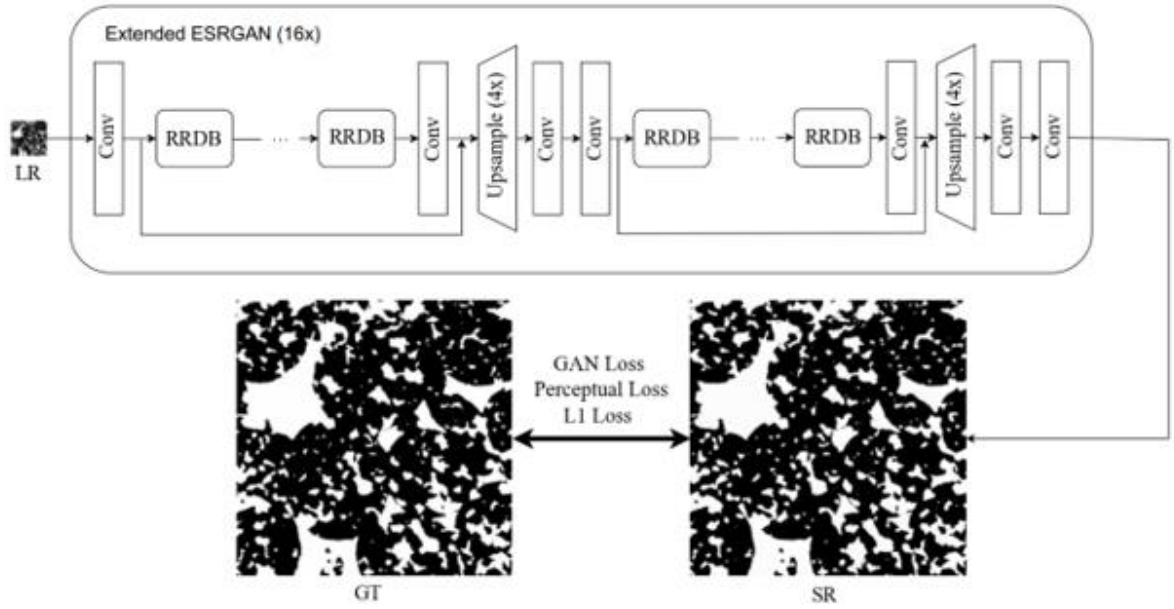

Fig. 8 Representation of the proposed extension to ESRGAN generator to support scale factor of 16

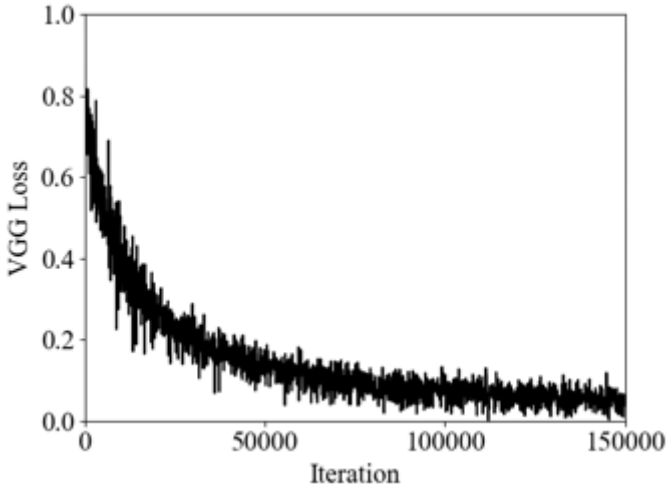

Fig. 9 VGG loss function during training the model

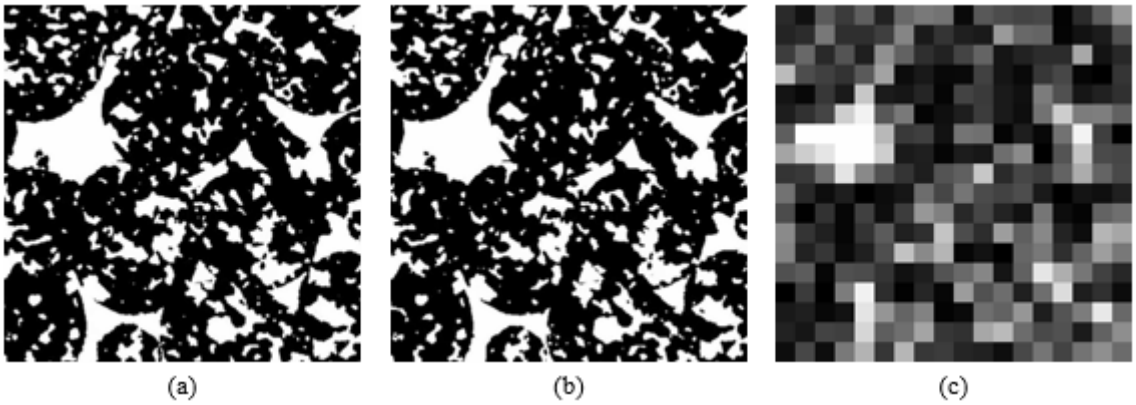

Fig. 10 (a) Original images (b) generated images from RealESRGAN (c) downsampled images, in multi-scale sandstone

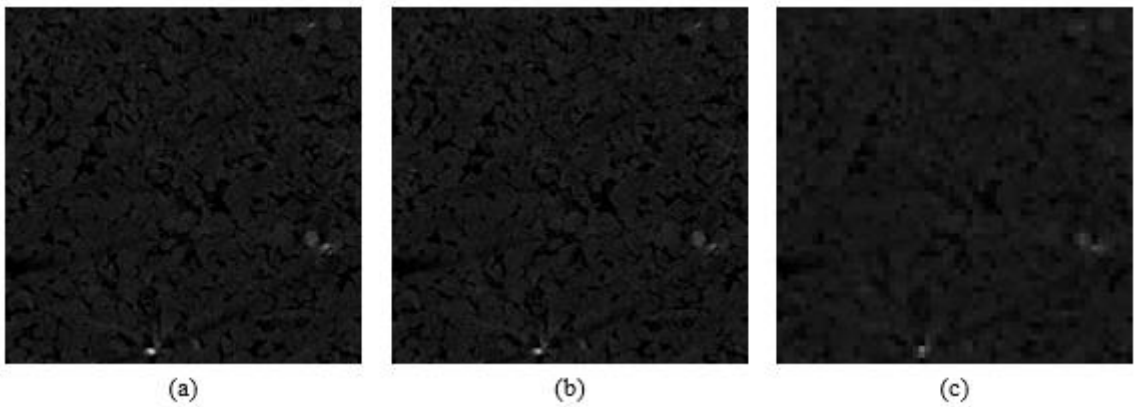

Fig. 11 (a) Original image (b) generated image from RealESRGAN (c) downsampled image, in Brea Sandstone

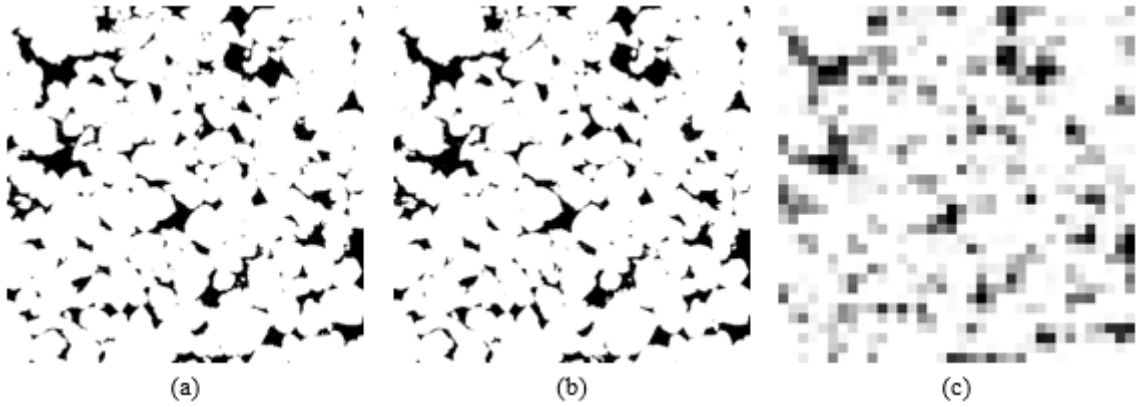

Fig. 12 (a) Original image (b) generated image from RealESRGAN (c) downsampled image, in Doddington sandstone

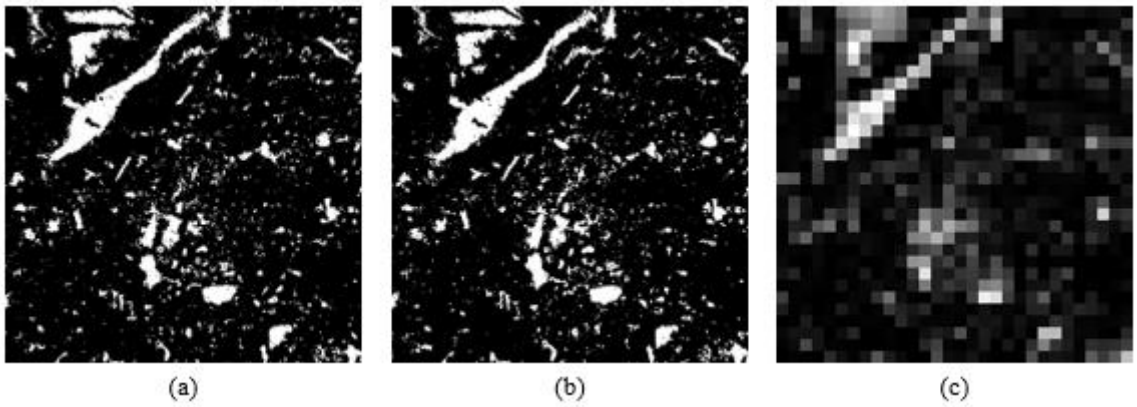

Fig. 13 (a) Original image (b) generated image from RealESRGAN (c) downsampled image, in tight carbonate

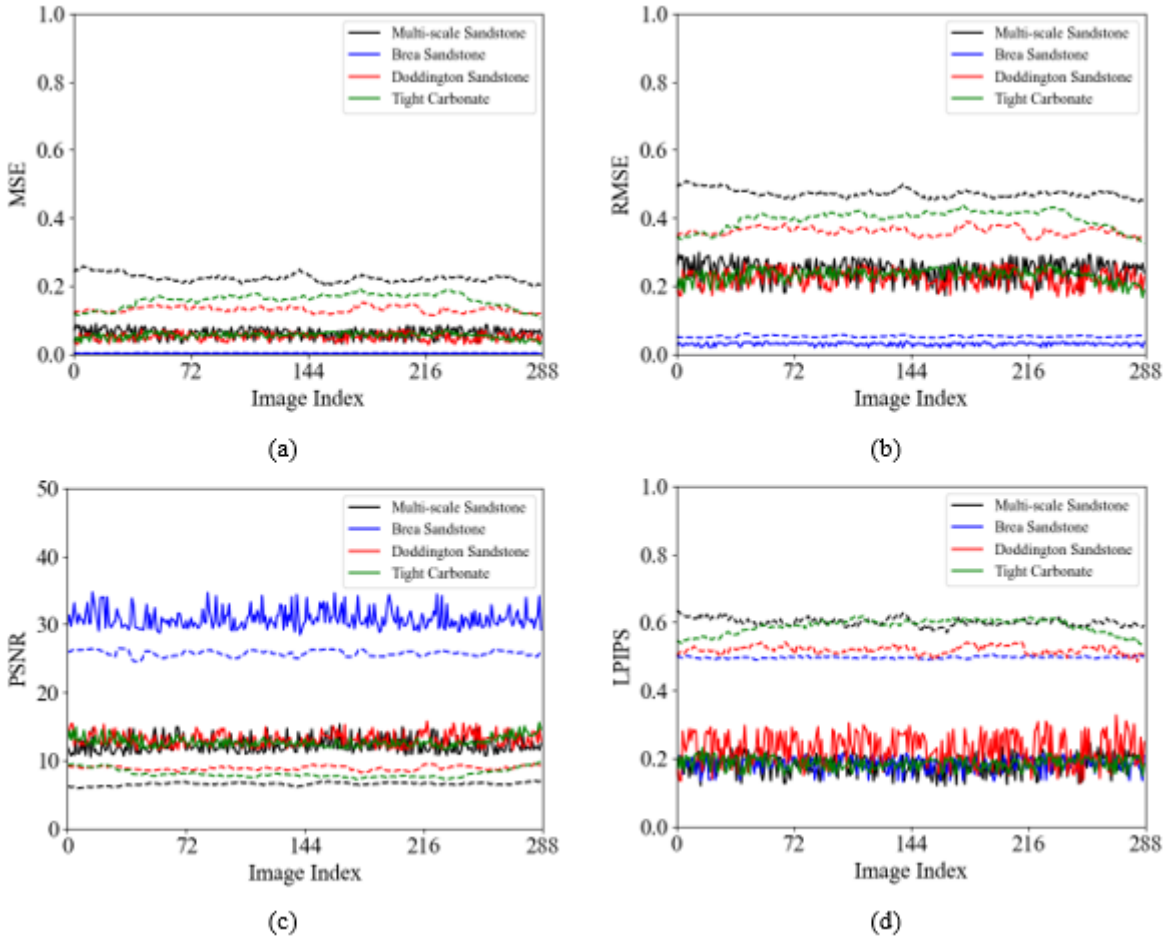

Fig. 14 Comparison between different evaluation metrics in multi-scale sandstone (solid lines: between high-resolution and generated images, dash lines: between high-resolution and low-resolution images)

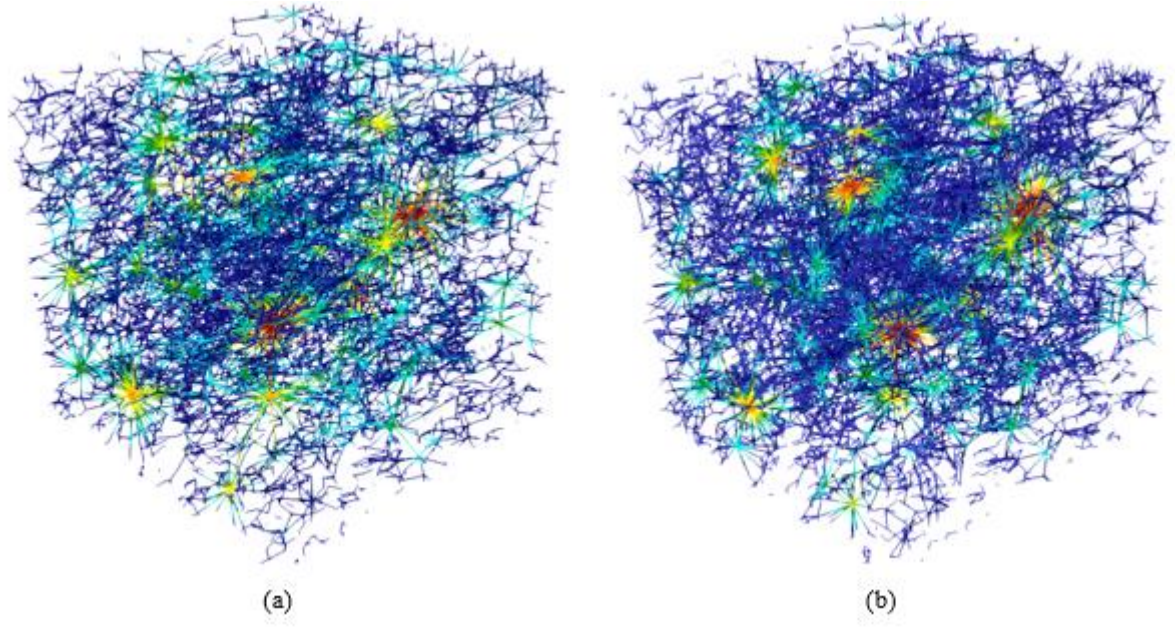

Fig. 15 Pore network model using (a) original images (b) generated images from trained model, in multi-scale sandstone

Tables

Table 1 All datasets used in our work

Table 2 Modified datasets for model training

Table 3 Network parameters for original, downsampled and generated network in multi-scale sandstone

Table 4 Flow parameters for original, downsampled and generated network in multi-scale sandstone

Table 1 All datasets used in our work

Number	Name	Resolution (μm)	Number of Images	Image Size	Related Work
1	Multi-scale Sandstone	3.00	512	300	Mohammadmoradi and Kantzas [65]
2	Brea Sandstone	2.25	1000	1000	Neumann et al. [66]
3	Doddington Sandstone	5.40	600	600	Moon et al. [67]
4	Tight Carbonate	30.60	500	500	Mohammadmoradi and Kantzas [65]

Table 2 Modified datasets for model training

Number	Name	Number of Training Images	Number of Testing Images	Real Image Size	Modified Image Size
1	Multi-scale Sandstone	672	864	300	288
2	Brea Sandstone	7120	2880	1000	960
3	Doddington Sandstone	1872	1728	600	576
4	Tight Carbonate	1060	1440	500	480

Table 3 Network parameters for original, downsampled and generated network in multi-scale sandstone

Network Parameters	Original Network	Downsampled Network	Generated Network
Porosity	0.24342	0.12435	0.24959
Pore Number	8416	325	9114
Throat Number	11754	308	12718
Average Coordination Number	2.79	1.89	2.85
Pore Volume (mm^3)	38.1435	21.4079	39.7425
Throat Volume (mm^3)	123.8119	61.3239	126.3147

Table 4 Flow parameters for original, downsampled and generated network in multi-scale sandstone

Flow Parameters	Original Network	Downsampled Network	Generated Network
Permeability (mD)	630.28	۴۱۸/۲۲	657.34
Volumetric Flow Rate (mm^3/min)	0.032595	0.021628	0.033994
Darcy Conductivity (mm/min)	0.366128	0.24294	0.381847
Darcy Velocity (mm/min)	0.042768	0.028378	0.044604